Hydraulic properties of injection formations constrained by surface deformation

Manoochehr Shirzaei [a,*], Michael Manga [b], Guang Zhai [a,b]

[a] *School of Earth and Space Exploration, Arizona State University, Tempe, AZ, USA*
[b] *Department of Earth and Planetary Science, University of California, Berkeley, Berkeley, CA, USA*

A B S T R A C T

Wastewater injection over the past decade has increased seismicity in the central USA, in some cases accompanied by detectable surface uplift. Here, we use this uplift to constrain subsurface properties and pore pressure evolution. We apply an advanced multitemporal interferometric algorithm to 35 synthetic aperture radar images acquired by ALOS satellite over four years before the 2012 earthquake sequence in east Texas, where large volumes of wastewater are disposed at depths of ∼800 m and ∼1800 m. To solve for the hydraulic diffusivity of the injection layers, we jointly inverted the injected volume and uplift data, considering a poroelastic layered half space. We find diffusivity values of 0.3 ± 0.1 m^2/s and 0.7 ± 0.15 m^2/s for shallow and deep injection layers, respectively, which combined with seismically-derived bulk moduli yields permeability values of $5.5 \pm 2.6 \times 10^{-14}$ m^2 and $1.9 \pm 0.25 \times 10^{-13}$ m^2 for these layers, consistent with permeability range reported for Rodessa formation and well test values. Hydraulic conductivity determines the evolution of pore pressure and thus the origin and location of induced seismicity. This study highlights the value of geodetic observations to constrain key hydrogeological properties of injection layers and to monitor the evolution of the subsurface pressure change.

© 2019 The Author(s). Published by Elsevier B.V. This is an open access article under the CC BY-NC-ND license (http://creativecommons.org/licenses/by-nc-nd/4.0/).

1. Introduction

The recent increase in seismicity across the eastern and central USA in the vicinity of wells with high rate or volume of fluid injection suggests a link between seismicity and injection operations (Frohlich et al., 2014, 2010; Hornbach et al., 2015; Horton, 2012; Johann et al., 2018; Keranen et al., 2013; Rubinstein and Mahani, 2015; Walsh and Zoback, 2015). To understand the origins of induced seismicity and better manage fluid injection, efforts have been made to identify the underlying mechanism (Healy et al., 1968; Majer et al., 2007; Segall and Lu, 2015; Shirzaei et al., 2016), to characterize the links to shallow hydrogeology (Manga et al., 2016; Wang et al., 2017), and to characterize the associated time-varying hazards (Langenbruch and Zoback, 2016; Norbeck and Rubinstein, 2018; Petersen et al., 2018; Zhai and Shirzaei, 2018). The injected fluid perturbs the stress field (Segall and Lu, 2015), reduces the effective normal stress on nearby faults (Fan et al., 2016; Shirzaei et al., 2016) and can cause surface deformation detectable using the Interferometric Synthetic Aperture Radar (InSAR) and Global Positioning System (GPS) (Loesch and Sagan, 2018; Shirzaei et al., 2016; Vasco and Ferretti, 2005). It has also been shown

that local hydrogeology plays an important role in determining the magnitude distribution of induced earthquakes (Holland, 2013; McGarr, 2014; Pei et al., 2018).

Beginning in February 2012, the Timpson area, eastern Texas experienced elevated seismic activity for 16 months, which culminated in a M$_w$4.8 earthquake on 17 May 2012, the largest recorded event in the region (Frohlich et al., 2014). Years of brine disposal preceded the seismicity at nearby high volume Class II disposal wells, two of which lie directly above the earthquakes (Shirzaei et al., 2016). Using a poroelastic model constrained by time series of injected fluid and surface uplift, and assumed hydrogeological properties, Shirzaei et al. (2016) suggest that these earthquakes are induced due to increased pore fluid pressure. Here, we present a new analysis and validation of ALOS L-band SAR imagery acquired between 2007 and 2011. This period spans the entire archive of ALOS satellite data. However, surface deformation may continue beyond this period because of the ongoing injection operation. The temporal sampling rate of this dataset is twice that of Shirzaei et al. (2016) and yields a much higher accuracy for the estimated long-term deformation rates. Next, we employ a multi-layered poroelastic half-space model and through joint inversion of the uplift and injection data, we solve for the hydrological properties of injection layers, including hydraulic diffusivity and permeability. Such parameters are critical to determine fluid pressure
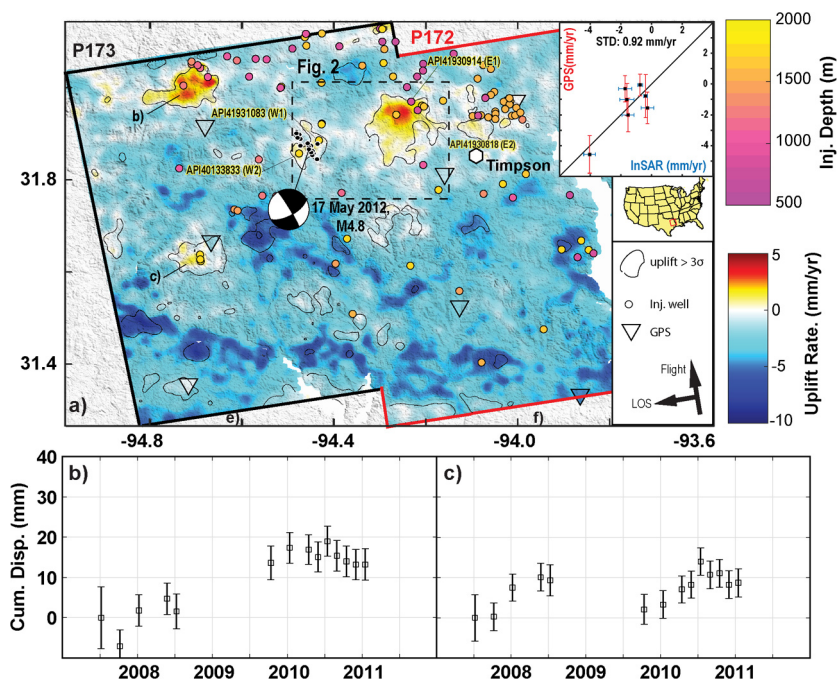
Fig. 1. a) Vertical velocity field estimated for Path 173 (black outline), Path 172 (red outline) and the overlapped zone for the period 2007/05/06-2011/02/14. SAR dataset includes 35 images acquired in the ascending orbit of the ALOS L-band satellite (heading angle = ∼345° and incidence angles = ∼34.5°degrees). Locations of seismicity and focal mechanism of the Timpson sequence are shown with black dots. Filled circles indicate the location of Class II wells in the region, color-coded with the depth of injection. W1, 2 and E1, 2 label four high volume injection wells near the seismic sequence, which are investigated by Shirzaei et al. (2016). The location of GPS stations is shown by triangles color-coded to their long-term vertical displacement rates. Zones of significant uplift rate with amplitude larger than 3σ errors are shown by black contours. Inset shows the bivariate plot comparing the InSAR-derived estimate of vertical displacement rate against that of GPS. The error bars indicate 1σ uncertainties. STD: standard deviation of difference between InSAR and GPS estimates. b, c) time series of cumulative LOS displacement at the two sites located west of Timpson, whose locations are marked in panel a. (For interpretation of the colors in the figure(s), the reader is referred to the web version of this article.)

changes in response to injection and thus control the associated seismicity rate change used in forecast models (Norbeck and Rubinstein, 2018; Zhai and Shirzaei, 2018).

2. Datasets and methods

2.1. Injection dataset

Fig. 1a shows the location of all Class II wells permitted within our study area. They are color-coded by the depth of injection, which ranges from ∼500 m to ∼2000 m. From this dataset, 21 wells are located within ∼20 km of the M_w4.8 earthquake and injected between 2007 and 2012 (see also Table S1). Four of these wells that are located in the vicinity of the earthquakes with an average injection rate of $8.9 \times 10^{+5}$ m³/yr are labeled by E1, 2 and W1, 2 in Fig. 1a. Within the Sabine Uplift of East Texas, these wells dispose of wastewater by injecting into Lower Cretaceous limestones (Granata, 1963). The geology of the region is further discussed in section 2.3.

2.2. Surface deformation

To measure the surface deformation near Timpson, we apply the Wavelet-Based interferometric SAR time series (so-called WabInSAR) (Shirzaei, 2013; Shirzaei and Bürgmann, 2013) to a dataset of 35 L-Band SAR images acquired in two overlapping tracks of ALOS satellite (Table S2 and Fig. 1a) in ascending orbit (Heading angle = ∼345° and incidence angles = ∼34.5° degrees). This data set includes 19 new acquisitions in addition to the dataset investigated by Shirzaei et al. (2016). While they used GMTSAR (Sandwell et al., 2011) for generating interferograms, here we use GAMMA software (Werner et al., 2000) to accurately co-register SAR images acquired in a given frame to their respective

reference image and generate 253 interferograms with perpendicular and temporal baselines smaller than 2000 m and 1500 days, respectively. This includes 167 and 86 interferograms in Path 172 and Path 173, respectively.

Applying a multilooking factor of 8 by 26 in azimuth and range directions yields a pixel size of ∼100 m × ∼100 m. The effects of a flat earth and surface topography are calculated and removed (Franceschetti and Lanari, 1999), using satellite ephemeris data and a 30 m Digital Elevation Model (DEM) provided by the Shuttle Radar Topography Mission (SRTM) (Farr et al., 2007). The elite (i.e., less noisy) pixels are identified by performing a statistical test, which investigates the time series of complex interferometric phase noise in wavelet domain (Lopez-Martinez and Fabregas, 2002; Shirzaei, 2013). The estimated interferometric phase noise associated with each pixel is also propagated through the time series analysis algorithm to calculate the standard deviation of the surface deformation time series and the velocity field.

The absolute estimates of the phase change are obtained by applying an iterative 2D sparse phase unwrapping algorithm (Costantini and Rosen, 1999). The effect of residual DEM error in each unwrapped interferogram is reduced using a low-pass filter that is generated based on Legendre polynomial wavelets (Shirzaei, 2013). The phase contributions from the topography-correlated component of atmospheric delay are estimated and removed using the approach developed by Shirzaei and Bürgmann (2012). This approach applies a 2D wavelet transform decomposing both DEM and unwrapped interferogram into their building blocks and then identifies the components with a significant correlation. Next, it down-weights the correlated coefficients and then performs the inverse wavelet transform to reconstruct the corrected unwrapped interferogram. We also correct all interferograms for the effects of orbital and satellite clock errors (Shirzaei and Walter, 2011). We then apply an iteratively re-weighted least squares method to obtain the time series of the surface deformation at the location of

each elite pixel as well as the associated variance-covariance matrix. This approach mimics the statistical properties of the L1-norm minimization because it is less sensitive to outliers resulting from improper phase unwrapping (Shirzaei, 2013).

Given that the system of equations is linear, the variance-covariance matrix is only a function of interferometric phase noise estimated above and the configuration of the network of interferograms, but independent from absolute phase values. Thus, the implemented filtering schemes within WabInSAR algorithm do not impact the variance-covariance matrix. Next, we apply a high-pass filter to reduce the temporal component of the residual atmospheric delay in the time series. This filter is designed based on continuous wavelet transforms and thus avoids shrinkage error (Shirzaei, 2013).

This approach is applied to data acquired in Path 172 and Path 173 separately. Interestingly, these two frames overlap in the Timpson area, and the region is, therefore, revisited by satellite about twice more frequently than elsewhere. In the overlapped zone more observations are available to adjust the errors and accurately constrain the long-term deformation rates. Combining the signal measured at the overlapping pixels, we implement the approach of Shirzaei (2015) to unify the references frames associated with overlapping SAR frames and reduce the errors due to the look angle differences. This is a physics-based approach that uses a Kalman filter to recursively align the deformation time series measured in Path 173 to that of Path 172 within the overlapped zone.

Next, we project the entire line-of-sight (LOS) velocities onto the vertical direction assuming that the horizontal components are negligible. This assumption is valid because differential horizontal motion estimated by GPS stations in this region is <1 mm/yr and thus is negligible. To avoid artefacts due to choice of an arbitrary local reference point, we use measurements of vertical land motion at the location of GPS stations provided by the Nevada Geodesy Lab (Table S3) and apply an affine transformation, including two rotations and one translation (Ojha et al., 2018; Shirzaei and Bürgmann, 2018). The measurements of GPS stations are provided in the North American Reference frame of 2012 (NA12) (Blewitt et al., 2013).

Fig. 1a shows the location of GPS stations as well as the long-term uplift rate in the NA12 reference frame. This transformation facilitates the validation of InSAR measurements against GPS observations. The inset in Fig. 1a shows the bivariate plot comparing the two data sets. We find that InSAR and GPS measurements agree well with a standard deviation of 0.92 mm/yr for their differences. The velocity map is dominated by negative values, indicating a large-scale sinking of the land surface, which is due to glacial isostatic rebound (Kreemer et al., 2018). At a smaller scale, the Carrizo-Wilcox aquifer, extending from the Louisiana border to the border of Mexico, experiences a long-term decline of groundwater near Timpson area during our study period (see groundwater level data at www.twdb.texas.gov/groundwater/) whose associated compaction may contribute to the observed subsidence.

We further narrow our focus to the areas with the statistically significant uplift signal. We select a conservative threshold of 3σ (σ is the standard deviation of the uplift rate) for the signal to be significant. Fig. S1 shows the spatial distribution of 3σ errors at the location of each pixel and black contours in Fig. 1a show the areas of uplift and subsidence rates with amplitude $>3\sigma$. This leaves us with three major zones of uplifts.

The most prominent anomaly is the signal investigated by Shirzaei et al. (2016). However, the amplitude of the signal detected here is ~20% larger and is more concentrated near the injection wells E1 and E2. Noteworthy, some uplift signal is also detected near the wells W1 and W2, which is absent in Shirzaei et al. (2016). The reason for these slight differences is that our current analysis is based on a much larger dataset, allowing a better

assessment of uncertainties and reducing the effect of environmental artefacts and inaccurate phase unwrapping.

The other two sites of significant uplift are located to the northwest and southwest of Timpson, labeled by letters (b) and (c) and whose time series are shown in Figs. 1b and 1c. Both sites are adjacent to injection wells. Path 173 that covers these sites has a gap of ~18 months starting in mid-2008 through end-2009. Despite the gap, site (b) shows a near-monotonic uplift through mid-2010, when it shows the maximum uplift of ~20 mm and then starts to decline gradually. The site (c) shows a slightly different pattern with its first maximum uplift of ~10 mm in mid-2008, culminating in ~17 mm of uplift in mid-2010. This change in behavior over the gap period should not be over-interpreted as it may be solely due to artefacts caused by a data gap. We note that many wells are not associated with uplift signals. Possible reasons include no or low volume and/or deep injection during our study period, as well as spatially variable hydrogeology. In the following, we focus our attention on the major uplift zone near the Timpson area.

The dashed-box includes the zone of prominent uplift rate near Timpson, whose close-up is presented in Fig. 2a. We also show the location of earthquakes, and the 13 nearby injection wells active between 2007 and 2012. Fig. 2b shows the time series of the monthly injected volume at each well, color-coded by the distance of wells from the center of maximum uplift marked by the white square in Fig. 2a. Fig. S2 provides the same injection time series color-coded to the average injection depth. Fig. 2c shows the time series of LOS displacement at the location of maximum uplift, which results from combining the measurements of two overlapping SAR frames. Time steps belonging to Path 172 are marked with red squares, and black squares show that of Path 173. The bars also indicate the 1σ errors for estimated displacement at each time step. Green curve in Fig. 2c shows the sum of the injected volume at wells labeled by E1, 2 and W1, 2 in Fig. 2a. The displacement time series shows two maxima, in early-2008 and mid-2010, and a minimum in early-2009. This pattern correlates well with that observed in the injected volume time series (green curve) with a time lag of ~3 months. This lag can be explained by pore pressure diffusion within a poroelastic medium, as discussed later. In Fig. 2c the blue curve shows the aggregated monthly volume at all injection wells within ~20 km of the $M_w4.8$ earthquake. Although some of the distant wells injected as high volume as the wells considered in the green curve, their contribution to the observed deformation is likely negligible. This is because the diffusion length is proportional to square root of injection duration times the diffusivity of the injection layer (Shapiro, 2015) and the reach of pore pressure front is limited (Segall and Lu, 2015).

2.3. Local geology

The geologic cross section of the study area is shown in Fig. 3 (Granata, 1963). The stratigraphic units are characterized by a gentle southwestward dip. The shallow wells inject in the Washita Group and Rusk formations, which are mostly composed of limestone and shale with permeability ranging between 0.3 mDarcy and 500 mDarcy (Balkey, 1989; Pollard, 1989). The deep disposal wells inject in the Rodessa formation, which includes Oolitic sand with a permeability of 10–650 mDarcy (Mancini et al., 2012). Both of these high permeability formations are located between layers with low permeability that form a barrier for disposed of brine (Fig. 3). The Washita formation is overlain by a layer of chalk and Marl couplets with permeability <0.05 mDarcy (Berg and Gangi, 1999). The lake Ferry formation composed of anhydrite and permeability of <0.06 mDarcy overlays the Rodessa formation. Herein, we simplify this interbedded geological cross-section into seven layers, representing a poroelastic axisymmetric multilayered half space, whose mechanical properties are provided in Table 1. We
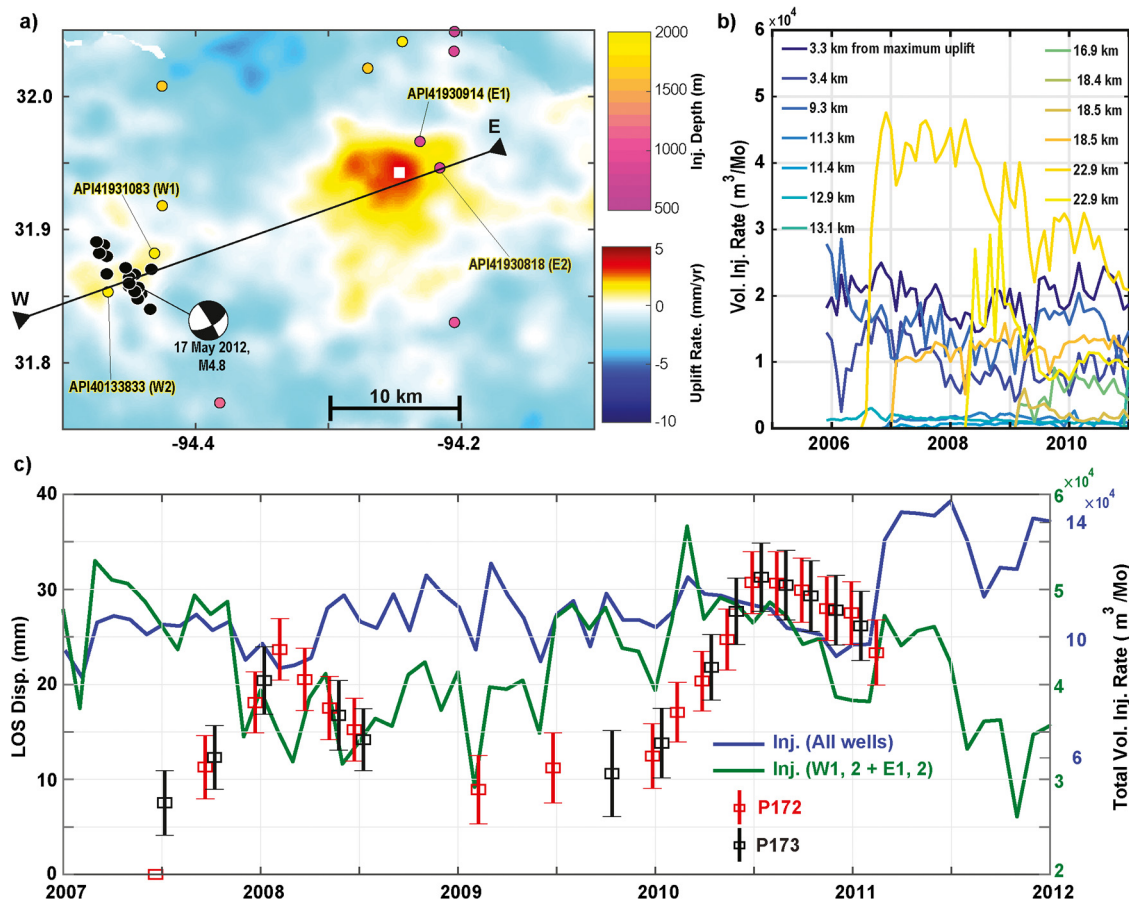
Fig. 2. a) Close-up view of the vertical velocity near the Timpson area. Locations of 13 injection wells active during 2007–2012 are color-coded with their injection depths. b) Time series of monthly injected volume at 13 active wells, color-coded based on their distance from the zone of maximum uplift at coordinate ($-94.25°$, $31.94°$) shown in panel a) with a white square. c) Time series of LOS displacement at the location of maximum uplift. Time steps associated with Path 173 and Path 172 are distinguished in red and black, respectively. Time series of aggregated injected monthly volume at wells E1, 2 and W1, 2 is shown in green and exhibits a good correlation with the LOS displacement time series with a ∼3-month lag. Also, time series of aggregated injected monthly volume at all wells within ∼20 km of the M_w4.8 earthquake is shown in blue.
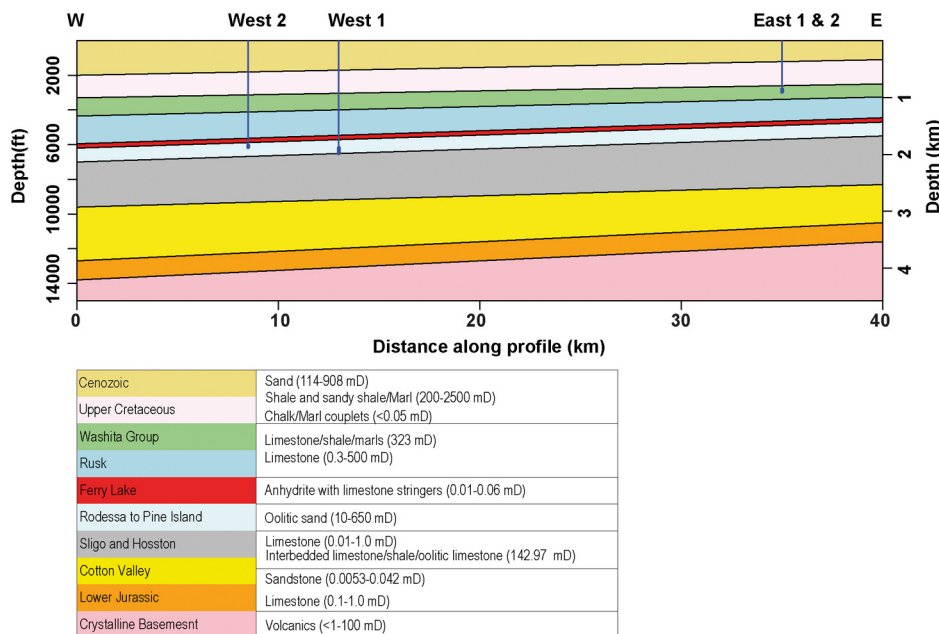

Fig. 3. Geological profile across the Timpson study area (line W-E in Fig. 2a) modified from Shirzaei et al. (2016). Vertical lines indicate the depth of injection wells. The formation rock type and the reported permeability values are also shown.

Table 1

Mechanical parameters of the poroelastic medium. ϑ = drained Poisson's ratio, ϑ_u = undrained Poisson's ratio, D = Diffusivity, B = Skempton ratio, ρ_w = Water density, E = Shear modulus.

Depth (km)	ϑ	ϑ_u	D (m²/s)	B	ρ_w (kg/m³)	E (Pa)
0-0.7	0.33	0.45	0.01	0.8	1000	10×10^9
0.7-1.0	0.33	0.45	0.1–5*	0.8	1000	10×10^9
1.0-1.6	0.23	0.45	0.01	0.8	1000	30×10^9
1.6-2.0	0.23	0.45	0.1–5*	0.9	1000	30×10^9
2.0-3.0	0.28	0.45	0.01	0.75	1000	30×10^9
>3.0	0.28	0.45	0.001	0.75	1000	50×10^9

* These ranges are input to the grid search and the final values of diffusivity are obtained following optimization.
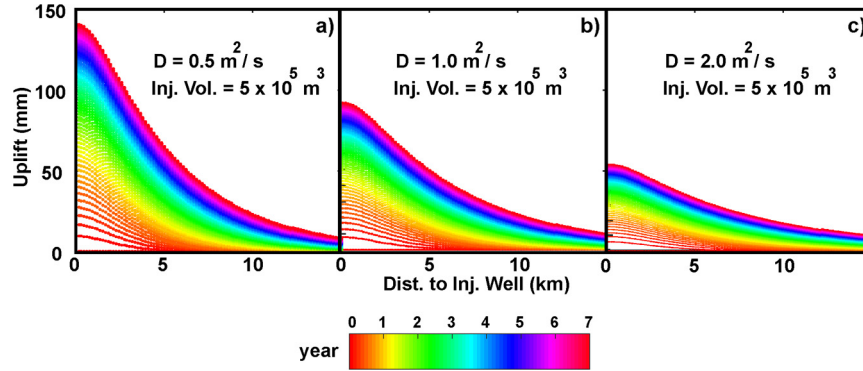

Fig. 4. Synthetic test showing the effect of hydraulic diffusivity (D) on surface uplift due to injection at a depth of 2.75 km. The horizontal axis is the distance from an injection well. The poroelastic model includes an impermeable layer between the surface and depth of 2 km and the permeable formation between 2 km and 3.5 km deep. Each panel shows the cumulative surface uplift over seven years following the injection begins versus the distance from the injection site.

set the shear modulus and Skempton ratio of each layer to a value that best represents rock properties associated with each formation after Wang (2000). The diffusivity of non-injection layers is set to a small value such that the injection layers are effectively sealed, consistent with the rock properties of overlying formations. The seismic velocity profiles near Timpson provided by Frohlich et al. (2014) are used to estimate undrained Poisson's ratio. The final velocity profile (Frohlich et al. (2014), Table S3) is obtained by solving the simultaneous hypocenter and 1D velocity model tomography problem for a set of earthquakes. Frohlich et al. (2014) do not report uncertainty for the final velocity model. Therefore, we assume a 20% uncertainty range for this model and propagate these uncertainties through the calculation to obtain the final uncertainty of the mechanical parameters that are estimated using this velocity model.

2.4. Poroelastic model inversion

The majority of studies of pore pressure diffusion and associated induced seismicity use geomechanical models whose parameters are based on geological or well test data (Fan et al., 2016; Hornbach et al., 2015), which are often uncertain. Among these parameters, hydraulic diffusivity controls the amplitude and reach of pore pressure changes, and is thus one of the critical factors determining the seismicity rate change within the area affected by injection (Zhai and Shirzaei, 2018). Knowing the injection history at a given well, the surface uplift caused by injection is inversely proportional to the hydraulic diffusivity of the injection formation. To clarify this point, we perform three synthetic tests using a uniform injection rate in the middle of a permeable formation ranging between 2 km and 3.5 km depth with a hydraulic diffusivity of 0.5, 1, and 2 m²/s. The other mechanical properties of this permeable layer are similar to those of Rodessa formation. We also take advantage of an existing numerical solution for a multilayered poroelastic half-space presented by Wang and Kümpel

(2003). This solution considers forcing through a point source (an injection well) and computes the surface uplift and pore pressure due to fluid injection. Fig. 4 shows the calculated uplift for each scenario over a period of seven years versus distance from the injection site. As seen, the maximum uplift is inversely proportional to the hydraulic diffusivity. This synthetic test suggests that given an injection history, we may be able to invert the surface uplift data to solve for the hydraulic diffusivity of injection layers. Focusing on the prominent uplift anomaly observed near Timpson (Fig. 2a), the input parameters for each layer are the drained (unchanged pressure) and undrained (unchanged fluid content) Poisson ratios, hydraulic diffusivity, Skempton's ratio, fluid density, and shear modulus. We fix all parameters but the hydraulic diffusivity. The fixed parameters are listed in Table 1, and the injection layers are confined to 700–1000 m and 1600–2000 m for the eastern and western wells, respectively. To identify the optimum hydraulic diffusivities, we perform a grid search that comprises 2500 model simulations for values between 0.1 and 5 m²/s. We only consider the injections at W1, 2 and E1, 2 wells for model simulations. First, not including all wells in the model simulations makes the inversion manageable because each simulation using 4 wells takes several hours to complete on a 2.4 GHz CPU. Moreover, given that pore pressure change dissipates rapidly with distance (Segall and Lu, 2015) and the diffusion length (Shapiro, 2015) during the four years period spanned by our deformation data, the contribution from high volume injection at the farthest wells (Fig. 2b) may be negligible.

As seen in Fig. 2a, the surface uplift rate has a complex pattern that cannot be explained entirely with an axisymmetric multilayered poroelastic model. The model is thus constrained by the general pattern of the deformation rather than detailed deviations from an axisymmetric pattern. This is achieved by minimizing the norm infinity of the difference between observed and modeled uplift rates. Note that norm infinity is not a statistically robust norm and its results can be affected by observation noise
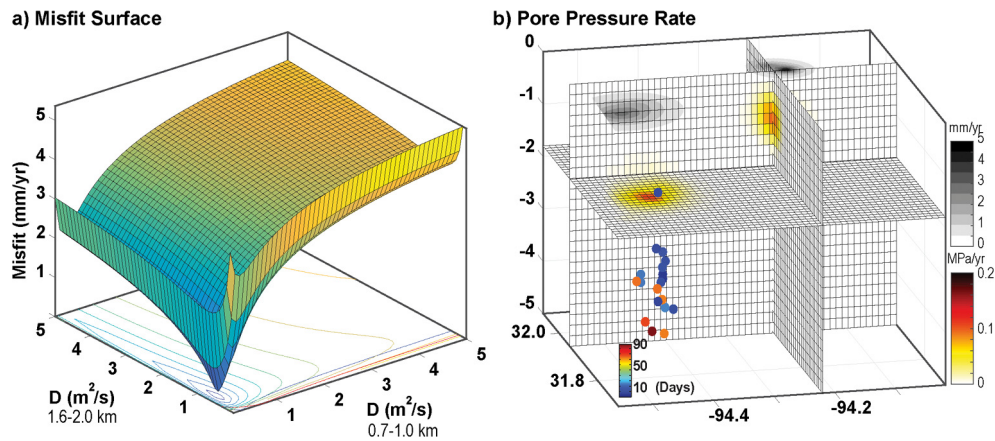
Fig. 5. a) Misfit surface showing the norm infinity of the difference between the observed and modeled uplift rates. b) Pore pressure distribution for the model with optimum (smallest misfit) hydraulic diffusivities. The associated uplift rate is shown using the gray colorbar on top. The location of the Timpson earthquake sequence is color-coded with the occurrence date relative to the first event.

(Cadzow, 1973; Mikhail and Ackermann, 1982). Here, we validated its results using that of L1-norm minimization and find a similar set of parameters given the range of errors.

3. Inversion results

To obtain the optimum hydraulic diffusivity, we use the uplift rate shown in Fig. 2a and compare it with the predicted uplift rate from the poroelastic model for the same period spanned by the SAR data set. Fig. 5a shows the misfit ($\|observed-modeled\|_\infty$) surface. The global minimum has diffusivity values of 0.3 ± 0.1 m^2/s and 0.7 ± 0.15 m^2/s for shallow and deep injection layers, respectively. The uncertainties in the form of standard deviation are estimated through bootstrapping, where we repeated the grid search 250 times. In each iteration, the observations are perturbed using a synthetic random noise with a maximum amplitude equal to the observation 3σ error. Using these optimum parameters we set up the poroelastic model to calculate the evolution of pore pressure and surface uplift. Fig. 5b shows the distribution of pore fluid pressure change within the 3D medium during the period spanned by SAR datasets. We observe up to $\sim 0.2 \times 10^6$ Pa/yr pressure change near the injection wells, mostly adjacent to the W1, 2 and E1, 2 wells. The model also predicts up to ~ 5 mm/yr and ~ 3.5 mm/yr uplift near well E1, 2 and well W1, 2, respectively. The locations of earthquake hypocenters are also shown and are color-coded to the relative time of occurrence with respect to the first event in the sequence. These events are located within the network of temporary accelerometers and whose locations are considered reliable. Frohlich et al. (2014) report an uncertainty of ± 0.3 km for the epicentral locations and ± 0.6 km for the events depth. The downward migration of the seismicity is evident. Shirzaei et al. (2016) shows in their Fig. S9 that including the injection time series at additional wells has a negligible effect on the observed pore pressure change near the Timpson earthquake sequence.

4. Discussions

4.1. Impact of atmospheric delay on uplift rate

The troposphere and the middle atmosphere are the two layers comprising the shallow ~ 80 km of the atmosphere (Hanssen, 2001). Unlike the weather-free middle atmosphere, the troposphere is perturbed by near-surface vertical wind shear and by radiative heating (Hanssen, 2001). Variations in the tropospheric properties from 1st acquisition to 2nd can cause a change in length between the radar antenna and the resolution cells on earth. The

phase difference generated from an interferometric combination of these two images includes the so-called component of atmospheric delay in addition to the contributions from surface deformation. On the spatial scales of 10s m to 10s km, the atmospheric delay is mainly due to variations in the tropospheric water vapor, temperature, and pressure during the two image acquisitions (Hanssen, 2001). The tropospheric delay is commonly divided into stratified and turbulent components (Williams et al., 1998; Yu et al., 2017). The layered part correlates with topography, while the turbulent part (often due to severe weather conditions) has a chaotic spatiotemporal pattern (Yu et al., 2017).

The WabInSAR algorithm implements a variety of wavelet-based filters to mitigate the impact of atmospheric delay on the obtained deformation time series and velocity. There are other classes of correction methods that apply correction models informed by external data sets (Bekaert et al., 2015; Doin et al., 2009; Jolivet et al., 2011). To investigate the effectiveness of WabInSAR filtering scheme for reducing the impact of atmospheric delay, we test the correction model developed by Yu et al. (2018) and Yu et al. (2017). The model input includes estimates of GPS tropospheric delay at 5 min sampling rate, and high-resolution European Centre for Medium-Range Weather Forecasts data sampled every 6 hours at 0.125° spatial resolution and 137 vertical levels.

Fig. S3 shows the spatial distribution of estimated zenith atmospheric delay at the time of ALOS SAR image acquisitions. The absolute values of the delay are on the order of meters, and the stratified component of the delay dominates the signal. Note that for interferometric purposes only the relative variations of the delay in time and space are essential. Using the estimated delay and the interferometric pairs generated based on the real dataset, we produce a synthetic interferometric dataset. Next, we invert this synthetic dataset to solve for the time series and rate of atmospheric correction at the location of each elite pixel identified in the previous section. Fig. 6a shows the spatial distribution of the atmospheric correction rate. We also show the location of injection wells and the zones of confidence (Fig. 1a) based on the real dataset. The atmospheric correction velocity map is characterized by signals that mostly correlate with the topography and caused by the stratified component of the tropospheric delay. We find no significant correlation between the uplift rate obtained from WabInSAR processing of the real dataset (Fig. 1a) and that of atmospheric model (Fig. 6a). We further show the time series of atmospheric delay at the location of maximum uplift (Fig. 6b) compared with the time series of surface deformation obtained from WabInSAR processing of the real dataset (Fig. 2c). We find no correlation between these two time series as well. This atmospheric model
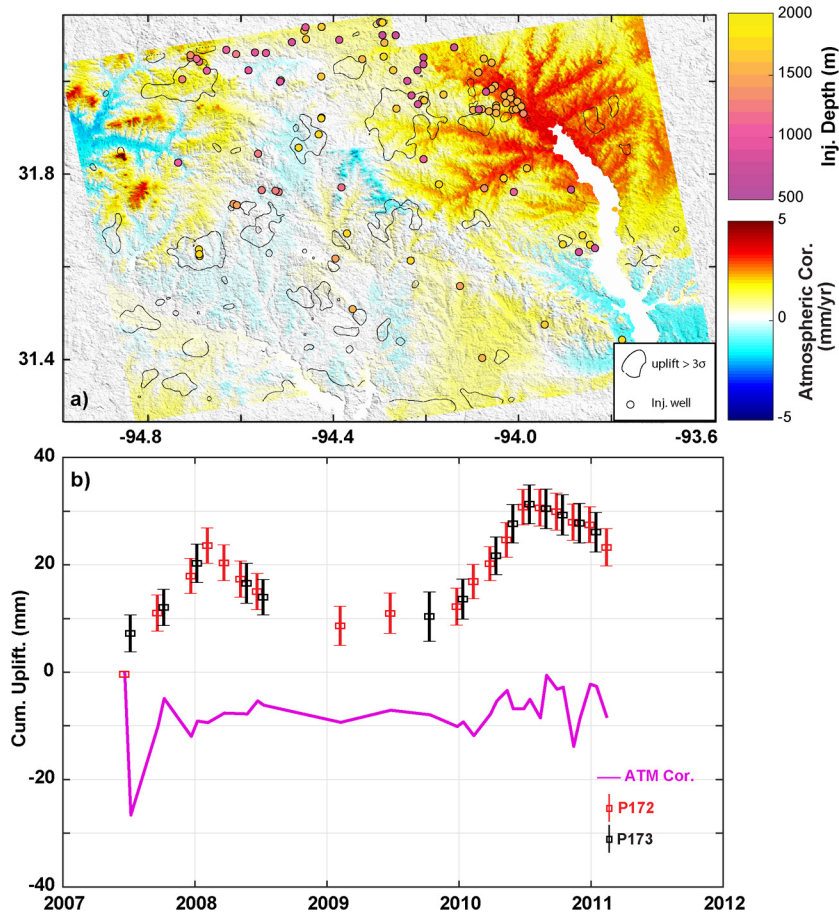
Fig. 6. a) Map of LOS delay correction rate in LOS direction estimated from the atmospheric model. Filled circles indicate the location of Class II wells in the region, color-coded with the depth of injection. Zones of the significant uplift rate with amplitude larger than 3σ errors are shown by black contours. b) Time series of LOS delay correction (purple) and LOS displacement (black and red) at the location of maximum uplift shown in Fig. 2a.

analysis in combination with the validation test against GPS data indicates that the WabInSAR filtering scheme is effective and the surface deformation data are robust.

4.2. Implication for fault orientation of Timpson seismic sequence

The aftershocks associated with the 17 May 2012 M_w 4.8 earthquake distribute along a 6 km long NW-SE linear trend consistent with the orientation of mapped basement faults (Frohlich et al., 2014) while the compilation of maximum horizontal stress orientations suggests that slip along NE direction is more favorable (Lund Snee and Zoback, 2016). To investigate whether our coupled poroelastic model calculation favors one orientation over another, we evaluate the Coulomb Failure Stress Change ($\triangle CFS$) associated with a change in pore pressure and poroelastic stresses at the depth of 2 km where seismicity initiated. We consider both orientations of NW-SE and NE-SW for the receiver fault. Fig. 7 shows the cumulative $\triangle CFS$ due to injection before May 2012, where positive $\triangle CFS$ promotes the rupture. We find that regardless of fault orientation $\triangle CFS$ is positive at the location of the 2012 earthquake sequence. This suggests that the pore pressure increase due to injection is the dominant factor triggering the Timpson seismic sequence. Therefore, given the NE-SW orientation of the maximum horizontal stress, either the pore pressure change is on the order of hydraulic fracturing pressure or the local stress field in eastern Texas (Lund Snee and Zoback, 2016) is more complex than previously thought.

4.3. Implication for hydrological properties

We used an inverse modeling approach to constrain the hydraulic diffusivity from surface deformation measurements, assuming a multilayered poroelastic half-space model. In recent work, Johann et al. (2018) proposed an alternative approach to account for the physical processes leading to induced seismicity in central Oklahoma. For this model to be applicable, an under-pressured unit is hydraulically connected to the underlying basement where seismicity is induced. Therefore, it does not provide the best framework for eastern Texas where the geology and injection history are different, even though it shows promise for modeling induced seismicity in Oklahoma.

Hydraulic diffusivity (D) is related to permeability (k), drained bulk modulus (K), Skempton coefficient (B), Biot-Willis coefficient ($\propto$) and viscosity (μ) through (Wang (2000), equation 4.63)

$$D = \frac{k}{\mu} \frac{KB}{\alpha} \tag{1}$$

where (Wang (2000), equation 3.75),

$$\alpha B = \frac{3(\vartheta_u - \vartheta)}{(1 - 2\vartheta)(1 + \vartheta_u)} \tag{2}$$

and ϑ and ϑ_u are the drained and undrained Poisson ratios, respectively. K is related to the undrained bulk modulus (K_u) through (Wang (2000), equation 2.22)

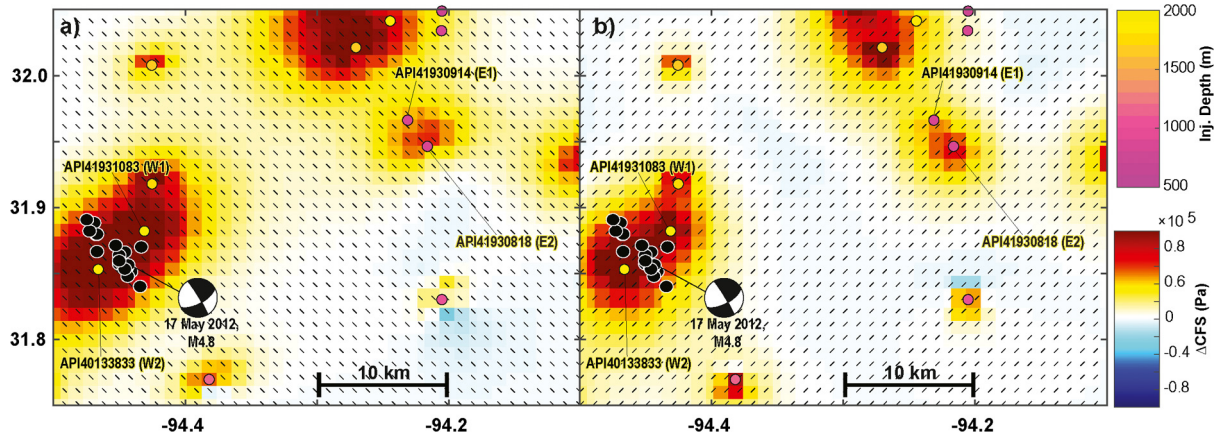$$K = K_u(1 - \alpha B) \tag{3}$$

Fig. 7. Cumulative Coulomb Failure Stress change due to an increase in pore pressure and poroelastic stresses associated with a fluid injection before May 2012. Positive color indicates that failure is promoted. a) NW-SE orientated receiver fault. b) NE-SW orientated receiver fault. Filled circles indicate the location of Class II wells in the region, color-coded with the depth of injection. Black lines show the orientation of the receiver fault.
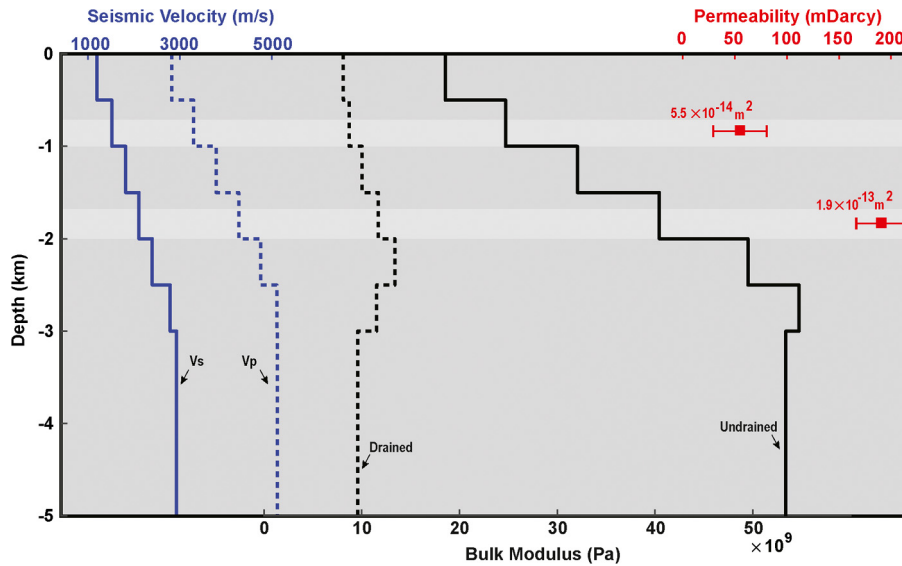

Fig. 8. Seismic velocity profiles from Frohlich et al. (2014) (blue lines), undrained (solid black line) and drained (dashed black line) bulk moduli, and the estimated permeability for the shallow and deep injection layers (red squares). The error bar shows the 1σ uncertainty for the estimated permeability.

The bulk modulus of porous materials depends on the boundary conditions, that is, the constraints on the control volume. The value K_u under undrained conditions (no change in fluid content) is greater than the value K under drained conditions (no change in pore pressure). Rocks are less compressible for undrained conditions because the fluid resists compression. Drained bulk moduli for typical sedimentary rocks are about 1/2 of the undrained value (Wang (2000), table C1). A bulk modulus can also be measured from seismic velocity. As the measurements are made at high frequency, typically 10-100 Hz, this dynamic bulk modulus ($K_{seismic}$), will approach the undrained value (Mavko et al., 2009). The dynamic bulk modulus, obtained from the P-wave (v_p) and S-wave (v_s) velocities and rock density (ρ) is

$$K_{seismic} = \rho\left(v_p^2 - \frac{3}{4}v_s^2\right) \qquad (4)$$

Fig. 8 shows the seismically-determined bulk modulus (thick black line) assuming $\rho \approx 2.7 \times 10^3$ kg/m^3 and the seismic velocity profiles near Timpson provided by Frohlich et al. (2014). Replacing Equation (2) in Equation (3), assuming $K_u = K_{seismic}$ and given the values listed in Table 1, the drained bulk moduli are also calculated and shown in Fig. 8 (dashed black line). Therefore, as-

suming the brine viscosity of $\mu = 1.1 \times 10^{-3}$ Pa s, Equation (1) yields permeability values of $\sim 5.5 \pm 2.6 \times 10^{-14}$ m^2 (55 ± 26.5 mDarcy) and $\sim 1.9 \pm 0.25 \times 10^{-13}$ m^2 (191 ± 24.8 mDarcy) for the shallow and deep injection layers, respectively (red squares in Fig. 8). The 1σ uncertainties are obtained following error propagation analysis (Mikhail and Ackermann, 1982) and assuming a 20% uncertainty for the seismic velocity profiles near Timpson provided by Frohlich et al. (2014). These values are consistent with those obtained through well drawdown tests in Ellenburger formation (Hornbach et al., 2015) and permeability range of 0.3–500 mDarcy reported for Washita Group and Rusk formation as well as 10–650 mDarcy reported for Rodessa formation (Fig. 3 and Fan et al. (2016)).

This study highlights the importance of monitoring surface deformation, specifically the high-resolution measurements obtained by advanced remote sensing techniques, to constrain governing field-scale poroelastic parameters of injection formations. These parameters determine the amplitude and rate of pore pressure changes, which in turn control the seismicity rate changes computed from physics-based induced earthquake models. We further suggest that this approach to be routinely applied to all sites of injection, where SAR data are available. Note that the lack of de-

tectable uplift can still be used to put a lower bound on the hydraulic diffusivity of the injection formation.

5. Conclusions

We show that the uplift signal due to fluid injection near Timpson, East Texas is robust. We further developed and applied an inverse modeling scheme that is informed by surface deformation and injection data and resolves the hydraulic diffusivity of the injection formations. This parameter is generally the most uncertain poroelastic and transport property. But it may significantly impact the estimates of hazards associated with induced seismicity because it controls the magnitude and spatial extent of pore pressure changes. Our estimates of permeability are consistent with those of other studies (but at larger spatial scales), highlighting the effectiveness of our approach for constraining the hydrogeological properties of injection formations, which in turn improves the accuracy of physics-based forecast models. The Coulomb Failure Stress Change associated with the optimum poroelastic model does not differentiate between NE-SW and NW-SE rupture orientations of the Timpson 2012 sequence, suggesting the pore pressure change is the driver of failure.

Acknowledgements

Appendix A. Supplementary material

Supplementary material related to this article can be found online at https://doi.org/10.1016/j.epsl.2019.03.025.

References

Balkey, J.P., 1989. Ann McKnight (Paluxy) field, Smith County, Texas. In: Shoemaker, P.W. (Ed.), Occurrence of Oil and Gas in Northeast Texas. East Texas Geol. Soc. Publ. Ser. East Texas Geological Society, Tyler, Tex., pp. 15–20.

Bekaert, D., Hooper, A., Wright, T., 2015. A spatially variable power law tropospheric correction technique for InSAR data. J. Geophys. Res., Solid Earth 120 (2), 1345–1356.

Berg, R.R., Gangi, A.F., 1999. Primary migration by oil-generation microfracturing in low-permeability source rocks: application to the Austin Chalk, Texas. Am. Assoc. Pet. Geol. Bull. 83 (5), 727–756.

Blewitt, G., Kreemer, C., Hammond, W.C., Goldfarb, J.M., 2013. Terrestrial reference frame NA12 for crustal deformation studies in North America. J. Geodyn. 72, 11–24.

Cadzow, J.A., 1973. A finite algorithm for the minimum l_∞ solution to a system of consistent linear equations. SIAM J. Numer. Anal. 10 (4), 607–617.

Costantini, M., Rosen, P.A., 1999. A generalized phase unwrapping approach for sparse data. In: Proceedings of the IEEE 1999 International Geoscience and Remote Sensing Symposium. IGARSS, Hamburg, pp. 267–269.

Doin, M.P., Lasserre, C., Peltzer, G., Cavalie, O., Doubre, C., 2009. Corrections of stratified tropospheric delays in SAR interferometry: validation with global atmospheric models. J. Appl. Geophys. 69 (1), 35–50.

Fan, Z., Eichhubl, P., Gale, J.F., 2016. Geomechanical analysis of fluid injection and seismic fault slip for the Mw4.8 Timpson, Texas, earthquake sequence. J. Geophys. Res., Solid Earth 121 (4), 2798–2812.

Farr, T.G., Rosen, P.A., Caro, E., Crippen, R., Duren, R., Hensley, S., Kobrick, M., Paller, M., Rodriguez, E., Roth, L., Seal, D., Shaffer, S., Shimada, J., Umland, J., Werner, M., Oskin, M., Burbank, D., Alsdorf, D., 2007. The shuttle radar topography mission. Rev. Geophys. 45 (2).

Franceschetti, G., Lanari, R., 1999. Synthetic Aperture Radar Processing. CRC Press.

Frohlich, C., Ellsworth, W., Brown, W.A., Brunt, M., Luetgert, J., MacDonald, T., Walter, S., 2014. The 17 May 2012 M4.8 earthquake near Timpson, East Texas: an event possibly triggered by fluid injection. J. Geophys. Res., Solid Earth 119 (1), 581–593.

Frohlich, C., Potter, E., Hayward, C., Stump, B., 2010. Dallas-Fort Worth earthquakes coincident with activity associated with natural gas production. Lead. Edge 29 (3), 270–275.

Granata, W.H., 1963. Cretaceous Stratigraphy and Structural Development of the Sabine Uplift Area, Texas and Louisiana. Shreveport Geological Society.

Hanssen, R.F., 2001. Radar Interferometry, Data Interpretation and Error Analysis. Kluwer Academic Publishers. 328 pp.

Healy, J.H., Rubey, W.W., Griggs, D.T., Raleigh, C.B., 1968. The Denver earthquakes. Science 161, 1301–1310.

Holland, A.A., 2013. Optimal fault orientations within Oklahoma. Seismol. Res. Lett. 84 (5), 876–890.

Hornbach, M.J., DeShon, H.R., Ellsworth, W.L., Stump, B.W., Hayward, C., Frohlich, C., Oldham, H.R., Olson, J.E., Magnani, M.B., Brokaw, C., 2015. Causal factors for seismicity near Azle, Texas. Nat. Commun. 6.

Horton, S., 2012. Disposal of hydrofracking waste fluid by injection into subsurface aquifers triggers earthquake swarm in Central Arkansas with potential for damaging earthquake. Seismol. Res. Lett. 83 (2), 250–260.

Johann, L., Shapiro, S.A., Dinske, C., 2018. The surge of earthquakes in Central Oklahoma has features of reservoir-induced seismicity. Sci. Rep. 8 (1), 11505.

Jolivet, R., Grandin, R., Lasserre, C., Doin, M.P., Peltzer, G., 2011. Systematic InSAR tropospheric phase delay corrections from global meteorological reanalysis data. Geophys. Res. Lett. 38.

Keranen, K.M., Savage, H.M., Abers, G.A., Cochran, E.S., 2013. Potentially induced earthquakes in Oklahoma, USA: links between wastewater injection and the 2011 Mw 5.7 earthquake sequence. Geology 41 (6), 699–702.

Kreemer, C., Hammond, W.C., Blewitt, G., 2018. A robust estimation of the 3-D intraplate deformation of the North American Plate from GPS. J. Geophys. Res., Solid Earth 123 (5), 4388–4412.

Langenbruch, C., Zoback, M.D., 2016. How will induced seismicity in Oklahoma respond to decreased saltwater injection rates? Sci. Adv. 2 (11), e1601542.

Loesch, E., Sagan, V., 2018. SBAS analysis of induced ground surface deformation from wastewater injection in East Central Oklahoma, USA. Remote Sens. 10 (2), 283.

Lopez-Martinez, C., Fabregas, X., 2002. Modeling and reduction of SAR interferometric phase noise in the wavelet domain. IEEE Trans. Geosci. Remote Sens. 40 (12), 2553–2566.

Lund Snee, J.E., Zoback, M.D., 2016. State of stress in Texas: implications for induced seismicity. Geophys. Res. Lett. 43 (19).

Majer, E.L., Baria, R., Stark, M., Oates, S., Bommer, J., Smith, B., Asanuma, H., 2007. Induced seismicity associated with enhanced geothermal systems. Geothermics 36 (3), 185–222.

Mancini, E., Aharon, P., Goddard, D.A., Horn, M., Barnaby, R., 2012. Basin analysis and petroleum system characterization and modeling Interior Salt Basins, Central and Eastern Gulf of Mexico, Part 3: Tectonic/depositional history, resource assessment. AAPG Search and Discovery Article #10395.

Manga, M., Wang, C.Y., Shirzaei, M., 2016. Increased stream discharge after the 3 September 2016 M-w 5.8 Pawnee, Oklahoma earthquake. Geophys. Res. Lett. 43 (22), 11588–11594.

Mavko, G., Mukerji, T., Dvorkin, J., 2009. The Rock Physics Handbook: Tools for Seismic Analysis of Porous Media. Cambridge University Press.

McGarr, A., 2014. Maximum magnitude earthquakes induced by fluid injection. J. Geophys. Res., Solid Earth 119 (2), 1008–1019.

Mikhail, E.M., Ackermann, F.E., 1982. Observations and Least Squares. University Press of America.

Norbeck, J., Rubinstein, J., 2018. Hydromechanical earthquake nucleation model forecasts onset, peak, and falling rates of induced seismicity in Oklahoma and Kansas. Geophys. Res. Lett. 45 (7), 2963–2975.

Ojha, C., Shirzaei, M., Werth, S., Argus, D.F., Farr, T.G., 2018. Sustained groundwater loss in California's Central Valley exacerbated by intense drought periods. Water Resour. Res. 54 (7), 4449–4460.

Pei, S., Peng, Z., Chen, X., 2018. Locations of injection-induced earthquakes in Oklahoma controlled by crustal structures. J. Geophys. Res., Solid Earth 123 (3), 2332–2344.

Petersen, M.D., Mueller, C.S., Moschetti, M.P., Hoover, S.M., Rukstales, K.S., McNamara, D.E., Williams, R.A., Shumway, A.M., Powers, P.M., Earle, P.S., 2018. 2018 one-year seismic hazard forecast for the Central and Eastern United States from induced and natural earthquakes. Seismol. Res. Lett. 89 (3), 1049–1061.

Pollard, N., 1989. Alabama Ferry (Glen Rose) field, Leon County, Texas. In: P.W. Shoemaker (Ed.), Occurrence of Oil and Gas in Northeast Texas. East Texas Geol. Soc. Publ. Ser. East Texas Geological Society, Tyler, Tex., pp. 1–14.

Rubinstein, J.L., Mahani, A.B., 2015. Myths and facts on wastewater injection, hydraulic fracturing, enhanced oil recovery, and induced seismicity. Seismol. Res. Lett. 86 (4), 1060–1067.

Sandwell, D., Mellors, R., Tong, X., Wei, M., Wessel, P., 2011. Open radar interferometry software for mapping surface deformation. Eos Trans. AGU 92 (28). https://doi.org/10.1029/2011EO280002.

Segall, P., Lu, S., 2015. Injection-induced seismicity: poroelastic and earthquake nucleation effects. J. Geophys. Res., Solid Earth 120 (7), 5082–5103.

Shapiro, S.A., 2015. Fluid-Induced Seismicity. Cambridge University Press.

Shirzaei, M., 2013. A wavelet-based multitemporal DInSAR algorithm for monitoring ground surface motion. IEEE Geosci. Remote Sens. Lett. 10 (3), 456–460.

Shirzaei, M., 2015. A seamless multitrack multitemporal InSAR algorithm. Geochem. Geophys. Geosyst. 16.

Shirzaei, M., Bürgmann, R., 2012. Topography correlated atmospheric delay correction in radar interferometry using wavelet transforms. Geophys. Res. Lett. 39 (1). https://doi.org/10.1029/2011GL049971.

Shirzaei, M., Bürgmann, R., 2013. Time-dependent model of creep on Hayward fault inferred from joint inversion of 18 years InSAR time series and surface creep data. J. Geophys. Res., Solid Earth 118 (1733–1746). https://doi.org/10.1002/jgrb.50149.

Shirzaei, M., Bürgmann, R., 2018. Global climate change and local land subsidence exacerbate inundation risk to the San Francisco Bay Area. Sci. Adv. 4 (3), eaap9234.

Shirzaei, M., Ellsworth, W.L., Tiampo, K.F., González, P.J., Manga, M., 2016. Surface uplift and time-dependent seismic hazard due to fluid injection in eastern Texas. Science 353 (6306), 1416–1419.

Shirzaei, M., Walter, T.R., 2011. Estimating the effect of satellite orbital error using wavelet-based robust regression applied to InSAR deformation data. IEEE Trans. Geosci. Remote Sens. 49 (11), 4600–4605.

Vasco, D.W., Ferretti, A., 2005. On the use of quasi-static deformation to understand reservoir fluid flow. Geophysics 70 (4), O13–O27.

Walsh, F.R., Zoback, M.D., 2015. Oklahoma's recent earthquakes and saltwater disposal. Sci. Adv. 1 (5), e1500195.

Wang, C.Y., Manga, M., Shirzaei, M., Weingarten, M., Wang, L.P., 2017. Induced seismicity in Oklahoma affects shallow groundwater. Seismol. Res. Lett. 88 (4), 956–962.

Wang, H.F., 2000. Theory of Linear Poroelasticity with Applications to Geomechanics and Hydrogeology. Princeton Univ. Press, Princeton, N.J., 276 pp.

Wang, R., Kümpel, H.-J., 2003. Poroelasticity: efficient modelling of strongly coupled, slow deformation processes in a multilayered half-space. Geophysics 68 (2), 705–717.

Werner, C., Wegmüller, U., Strozzi, T., Wiesmann, A., 2000. Gamma SAR and interferometric processing software. In: Proceedings of the ERS-Envisat Symposium. Gothenburg, Sweden, p. 1620.

Williams, S., Bock, Y., Fang, P., 1998. Integrated satellite interferometry: tropospheric noise, GPS estimates and implications for interferometric synthetic aperture radar products. J. Geophys. Res. 103 (B11), 27,051–027,067.

Yu, C., Li, Z., Penna, N.T., Crippa, P., 2018. Generic atmospheric correction model for interferometric synthetic aperture radar observations. J. Geophys. Res., Solid Earth.

Yu, C., Penna, N.T., Li, Z., 2017. Generation of real-time mode high-resolution water vapor fields from GPS observations. J. Geophys. Res., Atmos. 122 (3), 2008–2025.

Zhai, G., Shirzaei, M., 2018. Fluid injection and time-dependent seismic hazard in the Barnett shale, Texas. Geophys. Res. Lett. 45.